ELSEVIER

Contents lists available at ScienceDirect

# Geomechanics for Energy and the Environment

journal homepage: www.elsevier.com/locate/gete



# Quantitative assessment of well leakage, part I: Cement stress evolution

A. Moghadam\*, M. Loizzo

TNO Energy and Materials Transition, Utrecht, the Netherlands

### ARTICLE INFO

### Keywords: Well Leakage Well Integrity Shrinkage Microannulus Hydration Geothermal

### ABSTRACT

A damaged cement sheath in wells can open a leakage pathway to shallow freshwater aquifers and atmosphere. Quantitative assessment of leakage along wells has become an area of interest for both the industry and the regulatory bodies. The well leakage can be of importance in both active and legacy wells. In order to estimate leakage through cement sheaths, the size of the leakage pathway and the damage in the cement sheath must be estimated. In this work, we have developed a hydro-thermo-mechanically coupled near-well model that aims to calculate the evolution of cement's stress as it cures. This process takes into account the cement's gradual increase in stiffness, chemical shrinkage, and the heat of hydration. The results are verified using lab measured cement stress and pore pressure data from the literature. A case study was developed based on a low-enthalpy geothermal doublet in the Netherlands. The results show that during the cold water injection, an outer microannulus may open to 60 µm. The presence of an external source of water and formation stiffness are of significant importance in determining the damage to the cement sheath. The heat of hydration in cement increases the temperature of cement during curing. The subsequent drop in temperature due to drilling or completion reduces the cement stress and exacerbates the damage to the cement sheath. The producer well may not form a microannuli, however shear and cyclical failure may be of higher likelihood. The modelling framework presented here allows for estimation of annular cement stress in the well. The analysis provides quantitative estimates of the size of the leakage pathway along a well that can be used to estimate well leakge. Quantitative estimate of well leakage provides crucial information for quantitative risk analysis and provides a framework to optimize well operations to minimize leakage risk.

### Introduction

Zonal isolation in active and abandoned wells is paramount to ensure minimal fugitive methane emissions, to protect freshwater aquifers, to minimize pollution, and to prevent sustained casing pressures that in turn can lead to mechanical failure of well components. Wells penetrate different strata and can act as a leakage pathway in case of a damaged cement sheath. This has been linked to methane emissions to the atmosphere <sup>28,40</sup>, and aquifers <sup>32</sup>. Historically, oil and gas wells have been the main target of cement integrity research. The ongoing energy transition is expected to lead to drilling a significant number of geothermal, hydrogen and carbon storage wells. These wells are typically designed for a longer lifespan and have different operating conditions when compared to hydrocarbon producing wells. This creates the need to develop tools to improve cement integrity assessments.

The integrity of cement-casing-formation interfaces in a plug (for an abandoned well) or an annulus must be reasonably maintained to ensure

zonal isolation in wells. Cement can debond from the casing and/or formation to form a microannulus. The debonding occurs when the effective stress at the cement interface becomes tensile and overcomes the normal bond strength, if any is present. Presence of microannuli can provide a vertically connected, high-permeability fracture along the length of the wellbore, making it a higher leakage risk compared to other forms of failure <sup>44</sup>. Tensile cracks can form in a cement sheath when stress in the tangential direction surpasses the tensile strength of cement (Vrålstad, et al., 2019). Shear failure is another possible failure mechanism for cement. This occurs when the stress state in cement reaches the yield envelope. At low mean pressures, shear failure can be dilatative which is marked by crack development. At higher mean pressures, shear failure leads to a more ductile response and does not lead to a permeability increase <sup>13,41,6</sup>. The evolution of stress state in cement must be estimated to determine the probability and the mechanism of cement failure

Geomechanical models can be used to calculate stress changes in

<sup>\*</sup> Correspondence to: TNO Energy and Materials Transition, Princetonlaan 6, 3584 CB, Utrecht, the Netherlands. E-mail address: al.moghadam@tno.nl (A. Moghadam).

cement during the life of a well, typically using a staged finite element approach <sup>17,31,53,8</sup>. These models initialize the in-situ formation stresses around the wellbore followed by placement of cement between the casing and the formation. However, the initial stress state of cement after placement and curing is not known <sup>26,39</sup>. Therefore, the starting point for the geomechanical simulations is uncertain, rendering the rest of the analysis questionable. Literature studies have made various assumptions about the initial state of stress in cement after curing. These assumptions vary between zero <sup>46,8</sup>, formation pressure <sup>8</sup>, hydrostatic pressure of the slurry minus the pore pressure <sup>17,53</sup>, and hydrostatic pressure of the slurry <sup>14</sup>. These assumptions can all be justified under certain circumstances but there is no evidence to suggest which is the closest representation of reality or whether assuming a set initial stress value for all scenarios is appropriate.

Pore pressure in Portland cement drops significantly as hydration reactions progress<sup>21,37</sup>. Cement hydration also leads to bulk shrinkage<sup>37,49</sup>. The pore pressure drop, and the subsequent bulk shrinkage in cement have been considered as mechanisms that can lead to destressing in cement<sup>46,7,53</sup>. While cement's pore pressure drop has been confirmed experimentally in the past few decades, the stress change during the hydration process has only been measured recently. Meng et al.<sup>25</sup> reported the evolution of radial stress in a lab-scale cement plug during curing. Their results show a significant drop in radial stress and pore pressure. These tests are some of the first instances of cement stress drop being directly measured in the lab, to the best of our knowledge.

Cement hydration reactions are exothermic<sup>23</sup>. As hydration progresses, heat is released which increases the temperature of the cement and the surroundings. The impact of the heat of hydration is observed in field measurements, sometimes leading to a significant spike in temperature<sup>12,38</sup>. The increase in temperature can change the cement stress through thermal expansion of the cement, casing, and the formation. The heat of hydration will gradually dissipate, and the cement temperature will drop to the local geothermal gradient. This cooling effect could also impact the stresses in cement. This transient thermal effect coincides with a change in cement's mechanical properties as it hydrates. While the impact of the heat of hydration on temperature development has been studied in the literature, its effect on cement stress is not well-understood.

Zhang and Eckert<sup>53</sup> performed a staged finite element analysis on annular cement to estimate the near wellbore stress development. Their work considered the impact of the cement's pore pressure drop on its stress. However, pore pressure change was an input parameter, and not predicted by the model. Meng et al., 26 included the initial stress drop during curing in their stress calculations for a cement plug. However, their method relies on empirical correlations based on specific experimental results and thus may not be reliable for field-scale applications. Agofack et al., developed a chemo-poro-elastoplastic model of cement. Their model considers the hydration reactions and estimates the pore pressure and stress change. Using their methodology, the correct state of stress for cement during curing can be calculated. However, their model in the reported form cannot be used in a staged finite element framework to assess the long-term behavior of cement in a well. In addition, the mechanical impact of the heat of hydration of cement is not considered in the aforementioned studies.

In this work, we have developed a methodology to couple cement hydration reactions with a staged finite element model using a commercial package. The model is capable of predicting the expected cement pore pressure drop over time due to chemical shrinkage. Using the theory of poroelasticity, the subsequent stress drop in cement can be calculated. The impact of the heat of hydration is also incorporated in the model. The model is verified using the experimental data on cement stress by Meng et al.<sup>25</sup>. An earlier version of the methodology is presented by Moghadam and Loizzo<sup>27</sup>. Coupling cement hydration with staged finite element models creates a powerful tool capable of accurate estimates of cement stress evolution, in addition to other complex scenarios such as multiple casings, formation creep, eccentricity, cement

channels, etc., depending on the problem of interest. We developed a case study considering the stress development in a low-enthalpy geothermal well in the Netherlands to demonstrates the capabilities of the proposed modelling technique. The results provide invaluable insight on the behavior of plugs and annular cement, and the likelihood of debonding under in-situ conditions. The part II of the paper will focus on estimating potential leakage rates in wells with a case study for a Carbon Capture & Storage well (CCS).

### **Cement Hydration**

Portland cement is comprised of four principal components ( $C_3S$ ,  $C_2S$ ,  $C_3A$ , and  $C_4AF$ ). When mixed with water, each component displays different hydration kinetics and forms different products. Tricalcium silicate ( $C_3S$ ) is the main constituent with a concentration as high as 68 %, that forms calcium silicate hydrates (CSH) and calcium hydroxide (CH) upon reacting with water<sup>30</sup>. A simplified form of the reaction is shown in Eq. 1 (H in cement chemist notation stands for  $H_2O$ ).

$$C_3S + 5.3H \rightarrow C_{1,7}SH_4 + 1.3CH$$
 (1)

When the clinker is initially mixed with water, the ratio of water to solids is typically high and the cement mixture behaves like a slurry. As the hydration reactions continue, water is consumed, and different solid compounds are formed. The porosity of the material decreases and eventually a load-bearing skeleton forms. At this stage, cement changes its behavior from a slurry to a soft gel and eventually a porous solid. The point where the cement skeleton forms is typically referred to as the percolation threshold <sup>16,2</sup>. The extent of the hydration reactions is typically defined using the degree of hydration. This parameter ranges between 0 and 1, where 1 indicates that all the available clinker has reacted. In reality, different clinker phases react at different rates. For example, C3S typically reacts much faster than C2S<sup>30</sup>. However, for simplicity an average measure of the degree of hydration is used to represent the extent of the reactions for all clinker phases<sup>33</sup>.

Fig. 1 illustrates the progress of hydration reactions that eventually lead to a solid skeleton. Fig. 1a (on the left) indicates the moment when the clinker particles and water are mixed. The surfaces of the clinker grains will begin reacting with water to produce CSH (in yellow) and CH (in green). Fig. 1b in the center, shows the cement at percolation threshold, which likely occurs at a hydration degree between 0.05 to 0.2 (22; Agofack et a., 2019). The percolation threshold depends on the cement composition, presence of certain additives (aggregates or more active components in hydration), and w/c ratio<sup>22,7</sup>. At percolation threshold, the clinker, and hydration products have formed a connected network to a point where a soft skeleton has developed. The cement matrix has a high porosity and a low stiffness at this stage. Fig. 1c illustrates the material at its ultimate degree of hydration. Cement does not typically reach full hydration ( $\alpha = 1.0$ ) as the hydration products surrounding anhydrous clinker particles prevent further hydration. Hydration reactions continue at slow pace through diffusive flow of the available water in the macro pores. Ultimate hydration is expected to be in the range of 0.5 to 0.9 depending on the cement fineness, w/c ratio, and temperature<sup>23</sup>. At ultimate hydration, the permeability of the cement decreases substantially. The pore space available is small and poorly connected. The remaining water in the macro pores will likely be at a lower pressure due to chemical shrinkage. If the pressure drops below the saturation pressure of water, a fraction of the pore water could evaporate, leading to a partially saturated matrix.

All clinker phases undergo chemical shrinkage when they react with water. This means that the total volume of the reactants is higher than the volume of the products (Reddy at al., 2009;<sup>10</sup>). Chemical shrinkage represents the absolute (internal) volume change in the cement paste due to the hydration reactions. During the slurry phase, chemical shrinkage translates to an equal amount of bulk shrinkage as the slurry behaves like a liquid. Bulk shrinkage (or autogenous shrinkage) refers to the drop in the external volume of cement. Once the percolation

# Initial Condition Percolation Threshold Ultimate Hydration Water Clinker Hydrates Void Portlandite

Fig. 1. Schematic of the cement hydration process, from a slurry to a solid skeleton<sup>27</sup>.

threshold is reached, cement behaves like a poroelastic material. Hydration reactions remove water from the pores and deposit a smaller volume of hydration products. This effectively creates void space that causes the pore pressure to drop and compresses the newly formed cement matrix by increasing the effective stress. At this stage, bulk shrinkage of the cement becomes smaller than the chemical shrinkage (Bios et al., 2011). Pore pressure drop in a poroelastic material causes a change in the stresses and bulk volume. The molar volume of each clinker phase and the hydration products have been measured previously<sup>3</sup>. The chemical shrinkage coefficient of each clinker phase can be calculated through a volume balance between the reactants and the products for all the expected hydration reactions<sup>54</sup>. Table 1 summarizes the chemical shrinkage coefficient values for the main cement phases after Benz et al. (2005). In addition, the Bogue composition of the cement phases for class G cement is also provided in Table 1, based on Agofack et al., <sup>2</sup>. Eq. 2 can be used to calculate the theoretical chemical shrinkage (ml/g) for a cement paste at a hydration degree of 1.

$$R = \sum_{r} w_r R_r \tag{2}$$

In Eq. 2,  $w_r$  and  $R_r$  refer to the mass fraction and chemical shrinkage coefficient of the cement phase r, respectively. The theoretical chemical shrinkage of a cement paste depends on its chemical composition. However, the bulk shrinkage after the percolation threshold also depends on the thermo-poro-mechanical properties and the boundary conditions of the system.

Table 1 Chemical shrinkage coefficient (Benz et al., 2005) and total heat of hydration (Taylor, 1997) for the main cement phases. The Bogue mass fraction of the cement phases typical for class G cement is also provided<sup>2</sup>.

Cement phases	Bogue mass fraction	Chemical shrinkage coefficient (ml/g)	Total heat of hydration (J/g)
C <sub>3</sub> S	0.589	0.0704	500
$C_2S$	0.154	0.0724	260
C <sub>3</sub> A	0.023	0.1122	1150
C <sub>4</sub> AF	0.174	0.0802	420

### Methodology

This section outlines the details of the methodology used to couple cement hydration reactions with a geomechanical finite element model. A hydration model is used to calculate the rate of hydration over time for a specific slurry mix. The net water consumption/void creation is then estimated over time based on the shrinkage factors for cement phases. A homogenization model is developed to estimate the evolution of cement's mechanical properties with respect to the hydration degree. The aforementioned calculations are done using Python programing language. The mechanical properties and shrinkage results are imported into a hydro-thermo-mechanical model developed using the commercial finite element package Abaqus to calculate cement's stress evolution as it cures.

### Hydration degree

The degree of hydration is an indication of the extend of the clinker that has been consumed. This parameter controls the heat released during hydration, the amount of hydration products, the evolution of the mechanical properties, and the chemical shrinkage  $^{1,33}$ . Hydration rate is typically measured using the isothermal calorimetry method. This method involves measuring the cumulative heat release during cement hydration at a constant temperature. In order to model cement's mechanical behavior during curing, an estimate of the rate of hydration with time is required. The rate of the hydration reactions depends on the composition of the clinker, w/c ratio, temperature, pressure, salinity of the mix water, and the additives present in the slurry  $^{23,48}$ . The rate of hydration of cement can be estimated using Eq. 3.

$$\frac{\partial \alpha}{\partial t} = A_a \eta_a \exp(-\frac{E_a}{RT}) \tag{3}$$

In Eq. 3,  $\alpha$  is the degree of hydration,  $A_a$  is the chemical affinity,  $\eta_a$  is the permeability of hydration products,  $E_a$  is the apparent activation energy, and R and T are the universal gas constant and temperature, respectively. Lin and Meyer<sup>23</sup> proposed an approach to calculate the parameters in Eq. 3. Their methodology captures the impact of cement composition, w/c ratio, Blaine fineness, temperature, and pressure on the rate of hydration. Fig. 2 shows a comparison of the degree of

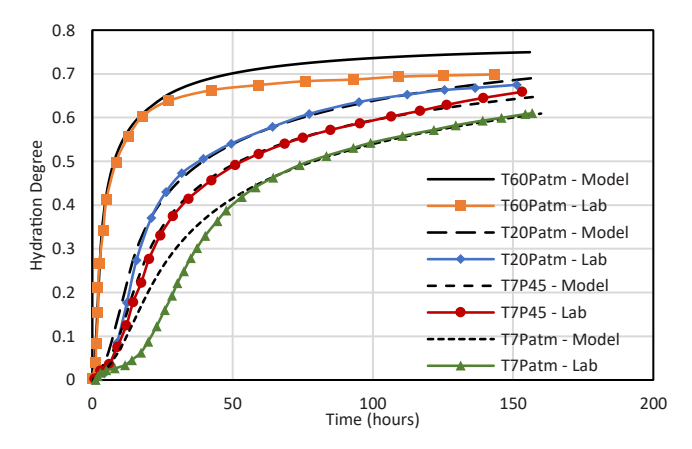


**Fig. 2.** Comparison of the hydration degree of class G cement over time from experiments and using Eq. 3 (w/c=0.44). T7P45 refers to the experimental temperature of 7 °C and pressure of 45 MPa. The measurements at 60 °C are reported by Pang et al.  $^{33}$  and the remaining experimental data is from Agofack et al.  $^{2}$ . The figure is derived from Moghadam and Loizzo $^{27}$ .

hydration of class G cement (w/c ration of 0.44) calculated using Eq. 3 with experimental measurements using isothermal calorimetry method  $^{2,33}$ . According to the data, temperature and pressure both increase the initial rate of hydration, with temperature having a more significant impact. The modelling results match the experimental data well. There is an overestimation of hydration degree by the model at 7  $^{\circ}\text{C}$  and atmospheric pressure during the initial 50 h of hydration. In addition, there is a slight overestimation of the hydration degree for measurements at 60  $^{\circ}\text{C}$ .

The degree of hydration can be related to the heat of hydration through Eq. 4:

$$\alpha(t) = -\frac{Q(t)}{O^0} \tag{4}$$

where,  $\alpha$  is the degree of hydration, Q is the cumulative heat measured over time, and  $Q^0$  is the total theoretical heat that will be released at full hydration.  $Q^0$  can be calculated using Eq. 5:

$$Q^0 = \sum_{r} w_r Q_r \tag{5}$$

where,  $w_r$  is the mass fraction and  $Q_r$  is the total heat of hydration of cement phase r. Table 1 provides the measured total heat of hydration for the main cement phases (Taylor, 1997). Class G cement from various suppliers could differ slightly in their phase composition. Therefore, the value of  $Q^0$  will vary depending on the cement supplier. However, the difference is relatively small. We calculated  $Q^0$  for four different class G cements reported in three different studies<sup>2,34,42</sup>. The results range between 415 and 435 J/g (per gram of clinker).

In this work, we use Eq. 3 to estimate the degree of hydration of Portland cement. Eq. 4 is then used to estimate the heat released over time due to the hydration reactions, assuming a  $Q^0$  of 426 J/g. The heat of hydration is treated as a heat source in the finite element model, to calculate the temperature and thermo-mechanical stress changes in cement.

# Mechanical properties

After the percolation threshold is reached, cement behaves as a poroelastic material. During the early stages, cement is a soft gel-like material due to its high porosity and water content. As hydration reactions continue, more water is consumed and the porosity decreases, while more solids are produced. This leads to an increase in cement's mechanical strength and stiffness. Cement's Young's modulus starts at a

low value immediately after the percolation threshold and increases to as high as 15 GPa at ultimate hydration<sup>1,18,43</sup>. With such a significant change in Young's modulus, the stress and pore pressure response of young cement will be significantly different from an aged cement. Therefore, to model cement's pore pressure and stress development during hydration, the evolution of the mechanical properties must be considered.

For a particular cement paste, the mechanical properties evolve with the degree of hydration. It is a cumbersome practice to measure the static mechanical properties of cement at different hydration degrees, and particularly difficult at a low degree of hydration. Teodouri et al., reported static Young's modulus of class G cement measured after 3 and up to 43 days of curing. Bourissai et al.9 reported dynamic Yong's modulus values for class G cement, using an Ultrasonic Cement Analyzer (UCA). Several studies have used micromechanical models and homogenization methods to estimate the evolution of the mechanical properties of cement<sup>1,15,19,35,4,9</sup>. These methods use the mechanical properties of the cement constituents and upscale them to produce an average macro-scale value of the mechanical properties. We simplified the approach described by Ghabezloo<sup>15</sup> to estimate the evolution of drained bulk and shear modulus of cement with hydration. The homogenized drained bulk modulus  $(K_d^{\text{hom}})$  and shear modulus  $(G^{\text{hom}})$  are calculated using Eq. 6 and Eq. 7<sup>47</sup>:

$$K_d^{\text{hom}} = \sum_{r} f_r k_r A_r^{\nu} \tag{6}$$

$$G^{\text{hom}} = \sum_{r} f_r g_r A_r^d \tag{7}$$

where,  $f_r$  is the volume fraction of the phase r at a given hydration degree.  $k_r$  and  $g_r$  are the bulk and shear moduli of the phase r, respectively.  $A_r^{\nu}$  and  $A_r^d$  are the volumetric and deviatoric strain localization coefficients, respectively. The strain localization coefficients can be calculated using Eq. 8, Eq. 9, and Eq.  $10^{51}$ :

$$A_r^{\nu} = \frac{\left[1 + \alpha_0 \left(\frac{k_r}{k_0} - 1\right)\right]^{-1}}{\sum_{r} f_r \left[1 + \alpha_0 \left(\frac{k_r}{k_0} - 1\right)\right]^{-1}}$$
(8)

$$A_r^d = \frac{\left[1 + \beta_0 \left(\frac{g_r}{g_0} - 1\right)\right]^{-1}}{\sum_{s} f_r \left[1 + \beta_0 \left(\frac{g_r}{g_0} - 1\right)\right]^{-1}}$$
(9)

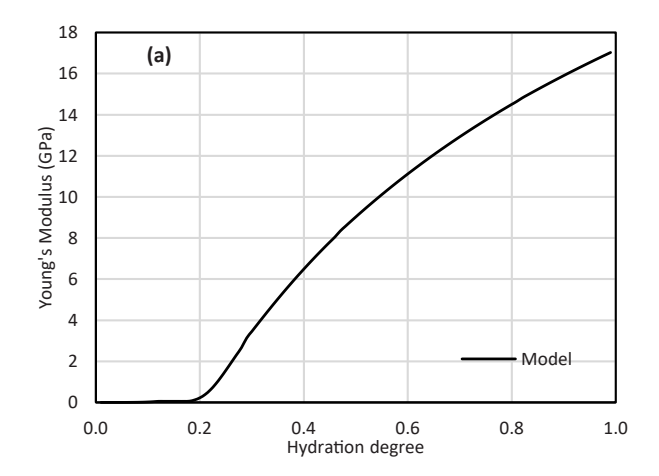
$$\alpha_0 = \frac{3k_0}{3k_0 + 4g_0}, \quad \beta_0 = \frac{6(k_0 + 2g_0)}{5(3k_0 + 4g_0)}$$
 (10)

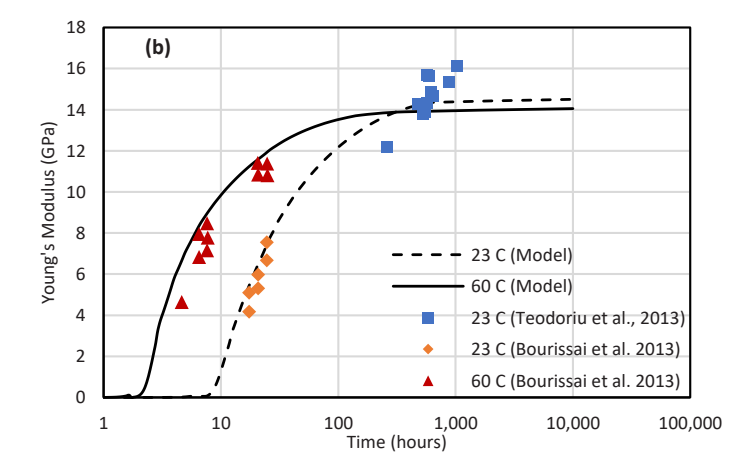
where,  $k_0$  and  $g_0$  are the bulk and shear modulus of the reference medium, respectively. We used the self-consistent homogenization scheme which assumes  $k_0$  and  $g_0$  to be equal to  $K_d^{\rm hom}$  and  $G^{\rm hom}$ , respectively. The Newton-Raphson numerical method was used to solve Eq. 6 and Eq. 7. The bulk and shear moduli can be used to derive Young's modulus and Poisson's ratio. For simplicity, we only considered CSH and CH as products. Additionally, high density and low density CSH were lumped together as one phase. Initially, only clinker and water were assumed to be present. At each hydration degree, the volume of clinker consumed and products that are formed was calculated. The volume fraction of each phase was then calculated using the hydration degree and the molar volume and density of each phase. Table 2 Summarizes the properties of the phases used to calculate the homogenized elastic properties of the cement paste.

Fig. 3 presents the predicted values of Young's modulus using the homogenization procedure. On the left (Fig. 3a), Young's modulus is plotted against the hydration degree. On the right (Fig. 3b), the values of the hydration degree are converted to time using Eq. 3, as depicted in Fig. 2. According to Fig. 3a, Young's modulus increases to 17 GPa at full hydration. The bulk and shear moduli of the phases of the cement paste

**Table 2**Summary of the parameters used to evaluate the elastic parameters with respect to the hydration degree.

		Reactants					Products			
Parameter	Unit	C3S	C2S	C3A	C4AF	CSH	CH	Void (porosity)	Source	
k	GPa	112	117	121	104	16	31	0	Constantinides and Ulm (2004); Ghabezloo <sup>15</sup>	
g	GPa	52	54	56	48	10	14	0	Constantinides and Ulm (2004); Ghabezloo <sup>15</sup>	
Specific gravity	-	3.21	3.28	3.03	3.73	2.11	2.24	0	Bentz et al. <sup>3</sup>	
Molar volume	cm3/mol	71.1	52.5	59.1	130.3	107.8	33.08	0	Bentz et al. <sup>3</sup>	





**Fig. 3.** On the left (a), Young's modulus predicted using the homogenization model versus the hydration degree. On the right (b), Young's modulus versus time predicted by the model, compared to experimental data<sup>27</sup>.

are assumed to be independent of temperature. Therefore, the relationship between Young's modulus and the hydration degree is also independent of temperature. However, Young's modulus versus time is a strong function of temperature, particularly at early stages of hydration. This is due to the significant impact of temperature on the hydration degree. The modelling results are compared to experimental data reported by Teodouri et al., 43 and Bourissai et al. 9. We converted the dynamic Young's moduli in Bourissai et al. 9 to static values using the correlation proposed by Lee et al. 20 for concrete, to facilitate comparison.

The Poisson's ratio ranges between 0.2 and 0.23 using the homogenization model. We assumed a constant value of 0.21 for the mechanical model. Biot's coefficient of cement has been shown to drop from 1.0 at percolation threshold to 0.6 at full hydration  $^1$ . We assumed a linear relationship between Biot's coefficient and the hydration degree which is a close approximation of the reported values by Agofack et al.  $^1$ . The friction coefficient between the casing and cement is assumed be zero initially, increasing linearly with the hydration degree to 1.0 at full hydration  $^{36}$ .

### Shrinkage

During hydration, clinker phases are consumed, and hydration products are formed. The definition of the degree of hydration broadly refers to the mass fraction of the clinker consumed. Therefore, the following coefficient can be defined to relate the volume change of the clinker to the change in degree of hydration<sup>1</sup>.

$$\delta_{ck} = \frac{1}{V_0} \left( \frac{\partial V_{ck}}{\partial \alpha} \right) = -\frac{1}{1 + w / c(\frac{\rho_{ck}}{\rho_w})}$$
 (11)

 $\delta_{ck}$  is negative, indicating a decrease in clinker volume with hydration. In Eq. 11,  $V_0$  refers to the initial volume of the slurry,  $V_{ck}$  is the volume of clinker,  $\alpha$  is the hydration degree, w/c is the initial water to cement ratio, and  $\rho$  refers to the density of clinker and water.

As clinker is consumed, total volume is lost due to chemical shrinkage. The chemical shrinkage volume can be conceived as void space that is created in the material. If the material behaves as a liquid, the void space drops the total liquid volume by the same amount. If the material behaves as a poroelastic medium, then the void space causes pore pressure drop, and a bulk volume change that is less than the initial void space, depending on the stiffness of the medium. The developed void space can be estimated using the chemical shrinkage coefficient of each clinker phase, according to Eq. 12:

$$\delta_{\nu} = \frac{1}{V_0} \left( \frac{\partial V_{\nu}}{\partial \alpha} \right) = -\delta_{ck} \sum_{r} \rho_r w_r R_r \tag{12}$$

where,  $\delta_v$  is the chemical shrinkage (void) coefficient,  $V_v$  is the chemical shrinkage volume (void volume),  $\rho_r$  is the density,  $w_r$  refers to the mass fraction of the clinker phase r (can be approximated by Bogue fractions), and  $R_r$  is the shrinkage volume per gram of the clinker phase r. Using Eq. 11 and Eq. 12, the rate of void creation due to chemical shrinkage can be calculated as the cement hydrates.

# Hydro-thermo-mechanical model

When the slurry is initially mixed, only clinker and water are present (ignoring the presence of additives in the current model). Hydration degree starts at zero and increases non-linearly with time according to Eq. 3. The cement slurry behaves as a liquid until the hydration degree reaches the percolation threshold. Up to this stage, the pressure and stress in cement are equal to the hydrostatic pressure of the cement column. Additionally, bulk shrinkage at this stage is equal to the chemical shrinkage (Eq. 12). The percolation threshold is estimated to range between 0.05 and 0.2<sup>1,22</sup>. After the percolation threshold is reached, cement becomes a poroelastic material. The hydration reactions continue to create void volume inside the cement pores due to chemical shrinkage. In the absence of an external water source, this void volume drops the fluid pressure in the cement pore space, which subsequently leads to bulk shrinkage as the effective stress of the medium

increases (while total stress decreases). Bulk shrinkage at this stage is due to the poroelastic response of the cement to pore pressure drop and is considerably less than the chemical shrinkage. Therefore, the theory of poroelasticity must be used to estimate the bulk shrinkage of cement and the resulting stress drop due to hydration reactions.

In this work, we used the commercial finite element software Abaqus coupled with the Python programming language to calculate the cement's pore pressure, stress, and volume change. Abaqus solves the momentum, fluid mass, and thermal energy equilibrium equations in a fully coupled manner. The analysis is divided into pre-percolation and post-percolation stages. In the pre-percolation stage, the cement's pore pressure and stress are equal to the hydrostatic slurry pressure. The volumetric shrinkage is equal to the chemical shrinkage. For the post-percolation stage, a mechanical model is generated using Abaqus. The geometry and the boundary conditions are selected based on the particular problem of interest (e.g., cement plug, annular cement, etc.). Initially, the cement's pore pressure and stress are set to the slurry pressure (effective stress of zero). This represents the instant that cement transforms from a liquid to a solid. Therefore, the pore pressure and stress are inherited from the liquid phase at the instant of transition.

The hydration degree and its rate are calculated versus time using Eq. 3. The impact of chemical shrinkage is incorporated in the mechanical model as a negative flow rate out of each cement element, i.e., a sink term, calculated using Eq. 13:

$$q_{\nu} = \delta_{\nu} V_{el} \frac{\partial \alpha}{\partial t} \tag{13}$$

where,  $q_v$  is the rate of void volume creation due to chemical shrinkage,  $\delta_{\nu}$  is the chemical shrinkage (void) coefficient calculated using Eq. 12,  $V_{el}$  is the volume of the cement element, and  $\frac{\partial \alpha}{\partial t}$  is the hydration rate at a given time. The Abaqus model only considers the cement behavior after the percolation threshold is reached. Therefore, the sink term  $(q_v)$  is only applied for the hydration period after the percolation threshold. This term simulates the void space created inside the matrix due to the hydration reactions, by removing an equivalent volume of water out of the pore space. The impact of external sources of water is ignored in the present study. This assumes that the analysis is conducted at the caprock level where the formation has negligible permeability. The pore pressure in cement is allowed to drop down to the saturation pressure of water. Once at saturation pressure, water evaporates, and the pressure remains relatively constant as the hydration reactions continue. Water evaporation can lead to multiple phases in cement pores. At low pressures (shallow depths), the vapor saturation can increase significantly (drying). This can drop the equivalent pore pressure in the cement due capillary forces, akin to a suction pressure<sup>29</sup>. This impact is limited to shallow depths and was ignored in this study.

A Modified Cam-clay plasticity model was used for cement's constitutive behavior. The yield surface is described in Eq. 14.

$$F = \frac{q^2}{M^2} + (p - p_t)(p - p_c) = 0$$
 (14)

In Eq. 14, q is the deviatoric component of stress, p is the mean stress,  $p_t$  is the strength if the material under hydrostatic tension, and  $p_c$  is the size of the initial yield surface in compression. Soustelle et al. <sup>41</sup> measured the MCC parameters for class G cement experimentally. Their reported values were used in this study. As hydration reactions progress, the plastic properties of the cement such as the shape and position of the yield surface will conceivably change. Therefore, modelling plasticity in a hydrating material is not straightforward, likely leading to a range of complex, uncertain, and time-dependent parameters. This topic is not covered here for brevity and will be discussed in another publication.

### Staged analysis

In order to estimate the evolution of cement stress for the case study,

a staged finite element analysis was designed which incorporates the aforementioned cement hydration and stress models as the hydration stage. The model generates a semi-2D finite element mesh representing the near-well region. Due to symmetry, only a quarter of the model is considered. Fig. 4 illustrates the geometry of the finite element model. The model consists of the casing (centered), cement, and the formation that extends 10 m away from the well. The size of the model was chosen to ensure the boundary effects are minimized. The model uses a plane strain boundary condition in the axial direction (no displacements in the axial direction). Both the casing and the formation are assumed to behave like linear elastic materials. The model calculates pore pressure, temperature, and displacements/stresses for all elements in a fully coupled manner. Fig. 5 presents a flowchart describing the steps to couple the cement hydration process with the staged FEA model.

The following stages are considered:

**Initialization stage**: In-situ effective stress, hydrostatic pore pressure, and temperature are assigned to the rock elements depending on the depth of analysis. The in-situ stress is transformed to the plane of the well.

**Drilling stage**: During this stage, the wellbore is excavated in the center of the model and the stress distribution around the wellbore is calculated after applying the mud pressure to the wellbore boundary. A transient heat transfer analysis is conducted to obtain the temperature distribution around the wellbore during the drilling stage. Temperature influences the stress values through thermal expansion of the materials.

Casing placement: After the drilling stage, a casing is inserted in the center of the wellbore. Mud pressure is applied at the inner face of the casing and slurry pressure is applied on the outside surface of the casing and the surface of the borehole (the annulus between the casing and the formation).

**Cement hydration**: Cement is placed in the annulus, assuming an initial cohesive bond to both formation and casing interfaces. The percolation threshold is equivalent to the moment that the cement acts as a solid with an effective stress of zero (stress equals pore pressure). Cement hydration is modelled following the methodology presented in the previous section where cement hydration degree, mechanical parameters, pore pressure and stress are calculated over time (waiting-oncement). This stage captures any potential pressure and stress changes in the cement in order to estimate the state of cement immediately after curing.

**Operations:** This stage models the operations of the well after cementing. This could include drilling the next leg of the well, completion operations, production, and injection. The operations are modelled as pressure and temperature conditions at the inner casing. For example, a change in mud density or downhole pressure is modelled as a pressure change inside the casing. Injection of cold  $CO_2$  is modelled as both a pressure and temperature boundary condition inside the casing.

### Verification

Recent experimental results by Meng et al.<sup>25</sup> were used to verify the proposed modelling technique. In the experiments, cement slurry was poured in a 2" ID casing (6.5" length). A 40 MPa axial load was then placed on the slurry using a load frame. A confining pressure of 25 MPa was applied to the outer surface of the casing. The cement's pore pressure was measured using pressure transducers at each end of the plug. The volumetric shrinkage was measured by monitoring the axial movement of the top ram. The major novelty of this work was the measurement of total stress at the cement/casing interface using sensitive strain gauges placed on the outer surface of the casing. The undrained test (experiment 1) in Meng et al.<sup>25</sup> was modelled in this work. The test used a class G neat cement with a water to cement ratio of 0.4, at room temperature.

The interface stress (radial stress), pore pressure, and the bulk shrinkage of cement are plotted in Fig. 6 along with the experimental data by Meng et al. <sup>25</sup>. The experimental results show an initial period of

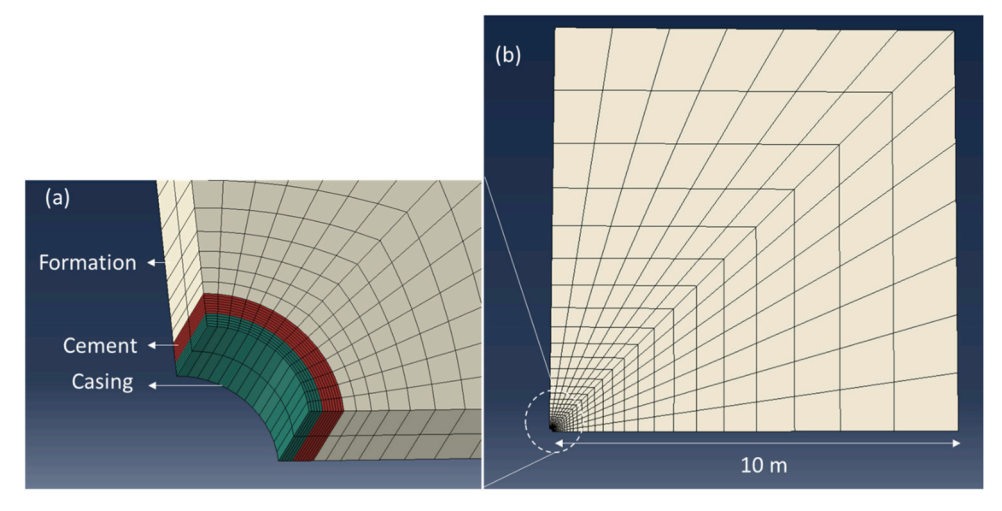


Fig. 4. The geometry of the semi-2D finite element model. Image (a) illustrates the casing, cement, and formation immediately around the wellbore. Image (b) shows the top view of the entire model domain which extends 10 m from the well.

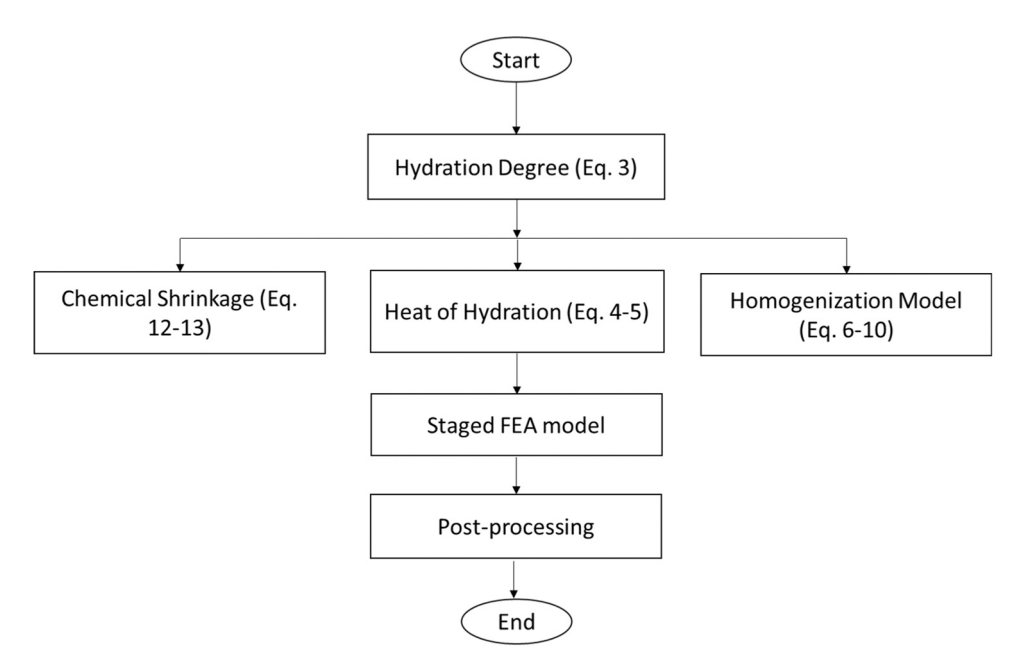


Fig. 5. A flowchart describing the methodology used to couple cement hydration with a staged FEA model.

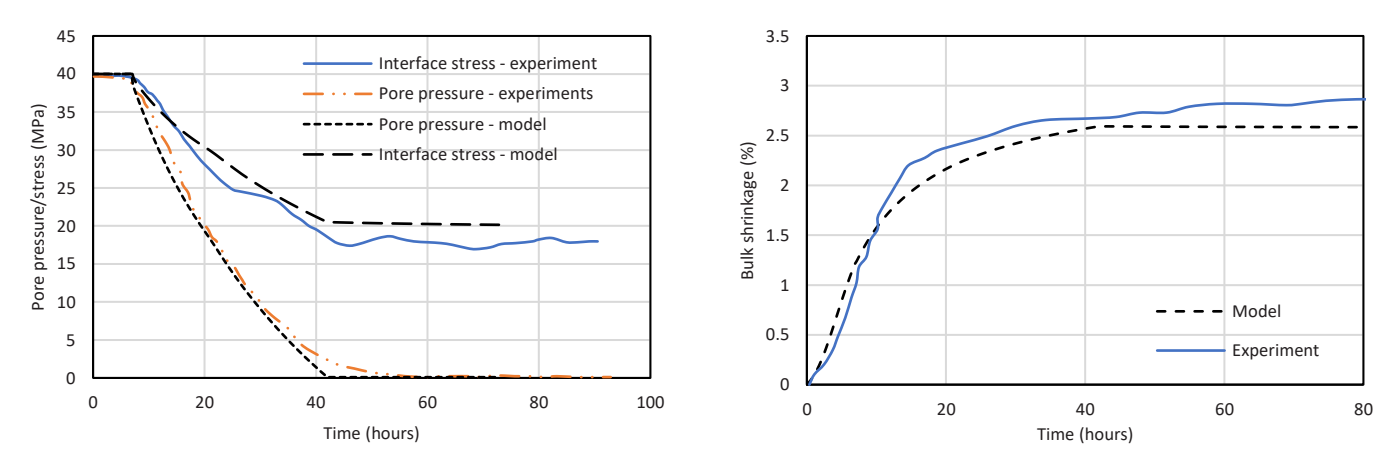


Fig. 6. Interface stress (radial) and cement pore pressure from the present model and experiments reported by Meng et al. 25.

approximately 7 h where the stress and pore pressure remain constant at 40 MPa. This period corresponds to the slurry state of cement. The bulk shrinkage results show that while pressure and stress remain constant, the slurry volume is decreasing at a rapid rate, indicative of chemical shrinkage. Once the percolation threshold is reached (after 7 h or hydration degree of 0.12), both the pore pressure and stress start decreasing. Pore pressure drops at a faster rate and ultimately reaches zero after approximately 60 h, with no external source of water available. The total stress at the cement/casing interface drops to approximately 17 MPa during the same period. Little change in stress is observed after the pore pressure reaches zero. Similarly, the shrinkage rate drops significantly after the pore pressure reaches zero. This is evidence that the bulk shrinkage in cement is a poroelastic response to pore pressure loss. Shrinkage rate does not reach zero but could potentially be explained by cement creep, which is ignored in this work. The results show a good match between the experimental and modelling results. The input parameters for the model are all described in the previous sections and are based on independent experimental measurements for class G cement.

### Case study

We have developed a case study inspired by a low-enthalpy geothermal doublet in the Netherlands. Both the injector and producer are assumed to have the same well construction. The well is comprised of a 13  $3/8^{\prime\prime}$  surface casing placed at a depth of 1241 m and cemented to the surface. A 9  $5/8^{\prime\prime}$  production liner is placed at a depth of 2030 m and cemented up to the liner hanger inside the surface casing (1118 m depth). The well schematic is shown in Fig. 7. Both wells are vertical along the surface casing and build a deviation angle of  $50^\circ$  along the production liner.

For this case study, the well integrity assessment is conducted using a semi-2D plane strain model at specific depths. Two models are developed for both the injector and the producer in the geothermal doublet. In an injector well, cold fluid causes the thermal fluctuation in the well. The change in temperature is more pronounced at greater depths as the temperature difference between the formation and the cold injected fluid is the highest at greater depths. Therefore, the maximum level of thermal shock is expected at the base of the liner. The well integrity analysis for the injector well is conducted at a depth of 2000 m, corresponding to the bottom of the production liner. The formation temperature is assumed to be 80  $^{\circ}$ C, and the injected cold fluid is assumed to be 30 °C at 2000 m depth. Table 3 presents the operational condition modelled after the cement placement. Once the liner is cemented, the final leg of the well is drilled into the reservoir. This period coincides with the cooling of the wellbore due to mud circulation. The circulating mud is assumed to be at 40 °C. During the completion stage, the circulation stops, and temperature is allowed to build up due to heat conduction from the formation. The injection then begins, marked by an increase in casing pressure and a drop in casing temperature due to cold fluid injection. Cold fluid is injected for 90 days, followed by a pause in injection for 30 days, and the resumption of the injection operation for another 80 days. The pause in operations was introduced to impose a cyclical load on the cement sheath which is expected to occur during regular operation of a geothermal doublet.

Contrary to the injection well, the production well experiences thermal stress due to producing hot fluids from deeper formations. The temperature difference is higher at shallow depths. Therefore, we conduct the well integrity analysis for the producer at a depth of 1200 m, close to the surface casing shoe. The produced fluid temperature is assumed to be 80  $^{\circ}\text{C}$ , while the formation temperature at that depth is 52  $^{\circ}\text{C}$  according to the local thermal gradient.

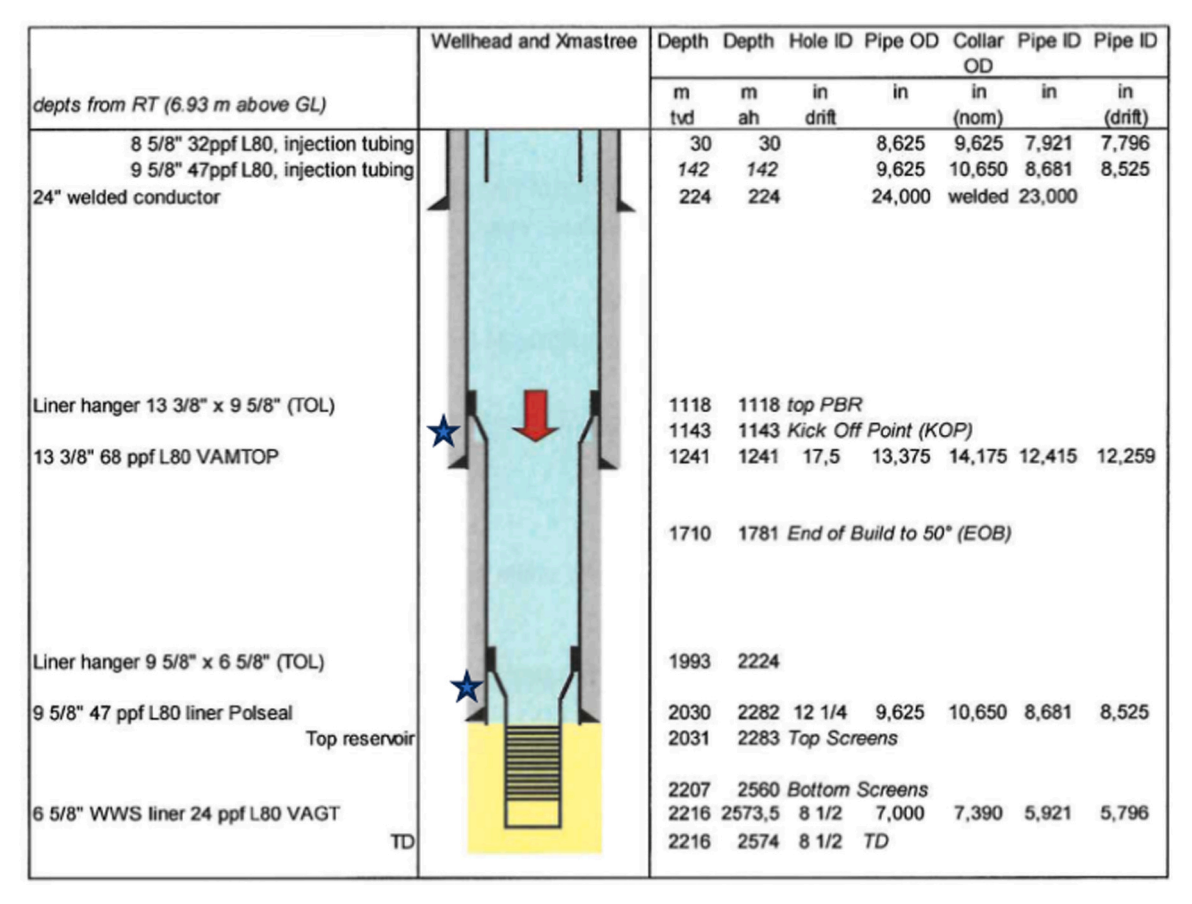


Fig. 7. The schematic of the well for the case study retrieved from www.nlog.nl. The stars show the depths at which the well integrity analyses were conducted at.

**Table 3**Summary of the operational conditions for the injector and producer wells.

Injector at 2000 m depth			Producer at 120			
Time after cementing	Casing Pressure	Casing Temperature	Time after cementing	Casing Pressure	Casing Temperature	Comments
Days	Pa	°C	Days	Pa	°C	
1	2.25E+ 07	40	1	1.35E + 07	30	Drilling the next leg
2	2.25E+ 07	40	8	1.35E + 07	30	
3	2.25E+ 07	Temperature change due to formation heat	10	1.35E+ 07	Temperature change due to formation heat	Completion
4	2.75E+ 07	30	11	9.70E+ 06	80	Production/injection begins
90	2.75E+ 07	30	90	9.70E+ 06	80	End of cycle 1
91	2.25E+ 07	Temperature change due to formation heat	91	1.35E+ 07	Temperature change due to formation heat	Pause in operations
120	2.25E+ 07	Temperature change due to formation heat	120	1.35E+ 07	Temperature change due to formation heat	
121	2.75E+ 07	30	121	9.70E+ 06	80	Production/injection resumes
200	2.75E+ 07	30	200	9.70E+ 06	80	

Table 4 presents the input parameters used for the well integrity analysis for the injector and producer wells. Wolterbeek and Hangx $^{50}$  reviewed the thermal properties of class G cement in the literature. They conclude that the thermal expansion of cement is close to  $1.3\times10^{-5}$   $1/^{\circ}\text{C}$  rather than  $10^{-5}$   $1/^{\circ}\text{C}$  which is typically assumed by other publications that focus on well integrity modelling. This means that the thermal expansion of cement is slightly higher than steel  $(1.2\times10^{-5}$   $1/^{\circ}\text{C})$ . This has important implications in terms of the thermal stress experienced by cement due to heating and cooling. The local stress at the wellsite was estimated from Mechelse $^{24}$ . All other well parameters from selected from www.nlog.nl for the BRI-GT-02 geothermal well. Cement mechanical properties were adopted from Soustelle et al.  $^{41}$ .

# Results

In this section, we present the well integrity results for the geothermal doublet analyzed for the case study. The results include the stress evolution in cement and its interfaces in the short term after placement and curing. In addition, long term stress path in cement

during the geothermal operations is demonstrated.

### Injection well

Fig. 8 presents the contact stress at the inner and outer surfaces of the cement sheath and the pore pressure immediately after placement. The cement interface stress values represent an average of radial stress at a cement interface. Pore pressure is also the average pore pressure in all cement elements Time zero represents the moment the analysis depth was drilled. The values in Fig. 8 start at the 24 h time mark as it was assumed that cement was placed 24 h after this depth was drilled. Immediately after placement, cement's pore pressure and contact stress are equal to the hydrostatic pressure of the slurry as indicated by the flat horizontal line at 24 h in Fig. 8a. The contact stress for the casing/cement interface is plotted as total stress and the stress on the formation/cement interface is plotted as an effective stress only to aid comparison. This means that the difference between the two stresses initially is equal to the formation (caprock) pore pressure which is 20 MPa. This means if the casing interface stress drops below 20 MPa, a microannulus

Table 4
Summary of the input data used for the well integrity simulations for the injector and producer wells. The blank entries for the producer indicate that the same value as the injector was used.

		Injector		Producer			
Parameter	Unit	Rock	Cement	Casing/other	Rock	Cement	Casing/other
Young's modulus	GPa	16	Calculated using Eq. 6 and Eq. 7	200	10	Same as injector	
Poisson's ratio	-	0.25	Calculated using Eq. 6 and Eq. 7	0.3			
Thermal conductivity	W/mK	2.1	1.0	50			
Specific heat	kJ/kgK	2000	1600	450			
Thermal expansion	1/K	1e-5	1.3e-5	1.2e-5			
MCC parameters	Dimensionless/	-	$\lambda = 0.02$	-			
	MPa		$\kappa = 0.0046$				
			M = 1.5				
			$P_{c} = 25$				
			$P_t = 3.7$				
Principal stresses/pore	MPa	$S_{11} = 29.4$	-	-	$S_{11} = 17.2$		
pressure		$S_{22} = 32.8$			$S_{22} = 19.2$		
		$S_{33} = 43.1$			$S_{33} = 25.1$		
		P = 20.2			P = 12.0		
Well inclination at depth	•	-	-	$Azimuth = 190^{\circ}$			Azimuth = 0 $^{\circ}$
				Inclination = $50^{\circ}$			Inclination = $0^{\circ}$
Analysis depth	m	-	-	2000			1200
Casing ID	mm	-	-	220.50			315.34
Wellbore diameter	mm	311.15	-	-	444.50		
Slurry SG	-		1.7	-		1.6	
Mud SG	-	-	-	1.15			1.15
Mud temperature	°C			40			30
Formation temperature	°C	80	-		52		
Cement top	m	-	1241	-		0	

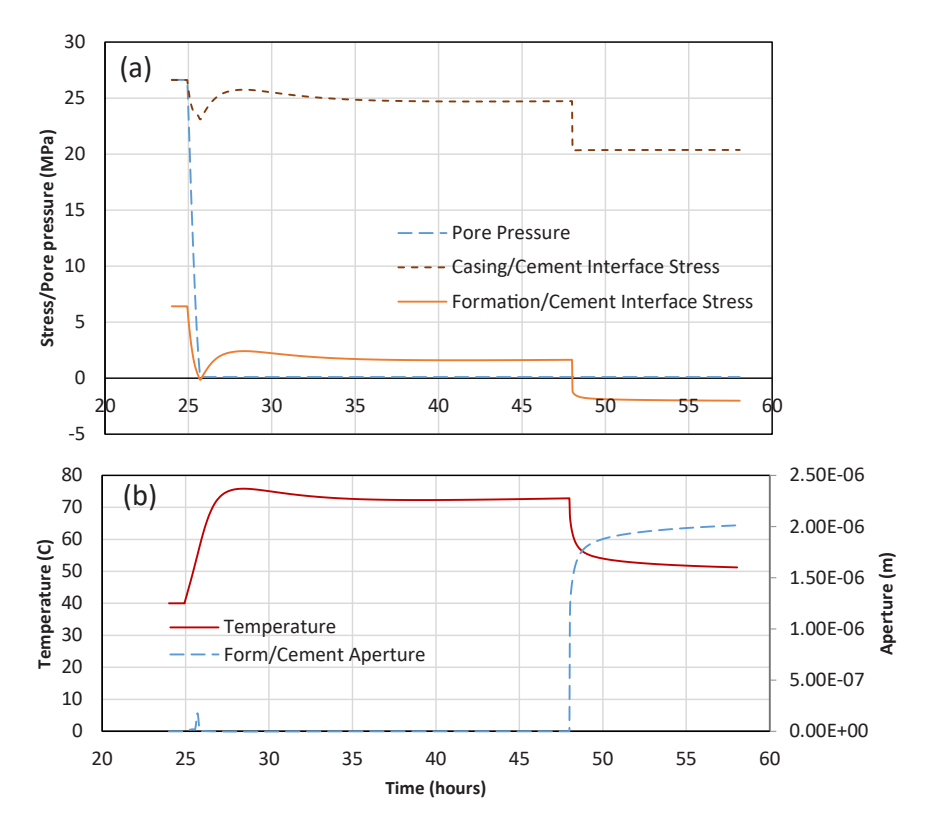


Fig. 8. The top plot (a) illustrates cement interface stresses and pore pressure for the injection well at early times. The bottom plot (b) shows the temperature evolution and the aperture at the formation/cement interface.

on that interface is possible, as formation fluid may open the interface. The cement's pore pressure and stress remain constant before the percolation threshold is reached. After the percolation threshold is reached, pore pressure in cement begins to fall due to hydration reactions and the presence of a poroelastic matrix. Cement pressure drops to zero at which partial evaporation of water is expected and subsequently the pressure remains at zero. During the pore pressure drop, cement stress at both interfaces drop. However, a larger stress drop occurs at the formation/cement interface. The stress drops to just below zero MPa which indicates a tensile stress regime. The bond strength of cement and formation is assumed to be 3 MPa. Therefore, no major debonding occurs after curing in this case. The formation interface stress rebounds to 2 MPa gradually. This is due to an increase in temperature from the heat of hydration. The interface stresses drop by nearly 5 MPa as the next leg of the well is drilled at the 48-hour mark. This is due to the cooling introduced by the mud circulation. This drops the formation/cement interface stress firmly in the tensile region at -2.0 MPa.

Fig. 8b shows the average cement temperature and the average micorannulus aperture at the cement/formation interface. During the pore pressure drop and subsequent stress reduction, a small aperture is observed on the outer interface for a brief period. It should be noted that the contact stresses are not homogenouous on the interfaces and only averages are shown here. The drop in stress leads to the debonding of a small portion of the outer interface. This shows up in the results as a small average aperture on the outer interface. The aperture closes as soon as the temperature increases. Cement temperature is assumed to be 40 °C immediately after placement (due to cooling from mud circulation). The temperature rebounds quickly during the waiting-on-cement period to 76 °C due to heat of hydration. Temperature drops as drilling continues which leads to partial debonding of the outer interface with an average aperture of 2  $\mu m$ .

During the operations of the geothermal injection well, cold fluid is introduced into the well. Fig. 9 shows the change in the injected fluid's temperature and the aperture of the microannulus over the entire

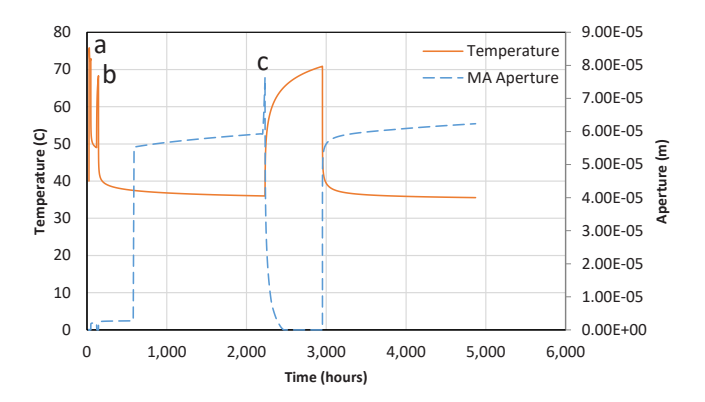


Fig. 9. Microannulus aperture and fluid temperature during the operational stage of the injection well.

simulated time. The temperature peak 'a' reflects the heat of hydration during the woc period. The temperature peak 'b' indicates the completion period when the mud circulation stops, and temperature builds up due to the heat conduction from the formation. Once the injection starts, temperature drops significantly and a microannulus opens on the outer cement interface with an aperture of approximately  $60 \mu m$ . The pause in injection is marked by a sudden drop in the bottomhole pressure which leads to a temporary increase of 20  $\mu m$  in the size of the microannulus, marked by point 'c'. However, as the temperature gradually builds up the microannulus fully closes. The resumption of injection reopens the microannulus to 60 um again. The microannulus can also be inflated or deflated by the pressure of the leaking fluid during the water injection. This effect is ignored in this work, implying that the water pressure near the wellbore will not increase significantly. Therefore, the microannulus size reported in Fig. 9 may be underestimated. The pressure dependence of the microannuli size will be covered in part II of this paper.

### Production well

Fig. 10 presents the cement interface stresses and pore pressure for the production well, immediately after cement placement. The results are at a depth of 1200 m for the cement sheath behind the surface casing. The formation pore pressure at this depth is expected to be 12 MPa. The results show that both cement interfaces lose some level of stress initially as the cement's pore pressure drops to zero. Similar to the injection well, the outer interface stress drops more than the inner interface (4 MPa versus 1 MPa). The stresses rebound as the temperature increases due to the heat of hydration. As drilling continues, the stresses drop again due to the cooling from the mud circulation. The stresses remain in the compressive region throughout this period with the inner interface at 4 MPa (effective stress) and the outer interface at 2 MPa. This indicates no debonding due to hydration and drilling of the surface casing.

The surface casing of the producer is exposed to a hot fluid during its operation. The increase in temperature in the vicinity of the well expands the casing and cement and increases the interface stresses. Therefore, debonding is not expected due to the production of hot fluids. Fig. 11 presents the change in fluid temperature and contact stress at the formation/cement interface. The interface stress drops to 2 MPa during the subsequent drilling operation. As production begins, the stress increases to 5.5 MPa in compression. The pause in production decreases the interface stress to nearly 4 MPa. The interface stress always remains compressive which indicates a low likelihood of debonding during the operation of the production well.

### Discussion

### Impact of water availability

Hydration reactions in cement lead to consumption of water, depositing solid products. Initially, the cement behaves as a slurry due to a high water to solids ratio. At this stage, fluid pressure and stress are equal until the percolation threshold is reached. In reality, cement forms gel strength even before the percolation threshold and the hydrostatic pressure drops due to friction as well. However, the drop was not considered in this work and the percolation threshold was modelled as an instant instead of a gradual strength development. After the percolation threshold, cement behaves like a poroelastic material. The pore pressure drop in cement results in a drop in its stress. In this work, we have shown that the stress change in cement can be modelled using the theory of poroelasticity, considering the hydration reactions and the gradual increase in the stiffness in cement. The input parameters in the model (hydration degree, elasto-plastic mechanical properties, phase shrinkage, and heat of hydration) are taken from independent lab

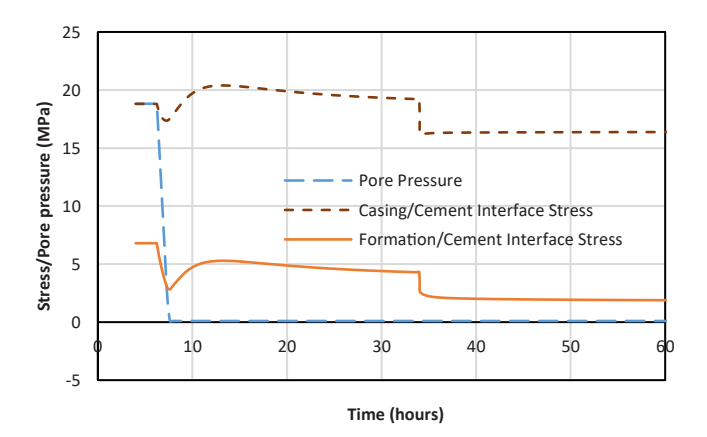


Fig. 10. Cement interface stresses and pore pressure for the production well at early times.

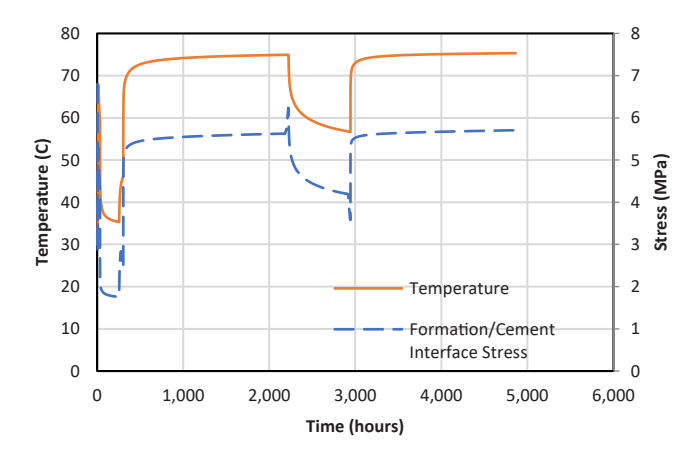


Fig. 11. contact stress and fluid temperature during the operational stage of the production well.

measurements which increases the confidence in the results.

The decrease in cement's total radial stress at interfaces increases the likelihood of debonding. Debonding occurs when the effective radial stress (total stress minus the pressure at the interface, which is assumed to be equal to the formation pore pressure in this work) at either interface becomes tensile and overcomes the bond strength. Effective stress is defined as total stress minus the fluid pressure. Fluid pressure can be supplied from the formation in contact with the cement, or from the high-pressure zones below. Disking cracks are common in a cement sheath which exposes the inner and outer interfaces to fluid pressure. Therefore, the decrease in total stress due to pore pressure drop in the cement matrix increases the likelihood of debonding. This explains why in some cases even the best cementing practices lead to a poor cement/casing bond according to sonic measurements.

When cement is placed against sealing formations, the external presence of water is limited during curing and therefore significant pressure drop is expected. However, against highly permeable formations the water encroachment can limit the pore pressure drop in cement. Zhang et al.<sup>52</sup> conducted lab experiments on cement plugs in contact with water on their outer surface. Their results indicate a pressure drop to 70 % of initial value for a 5 cm thick cement sheath after 50 h. Their experiment assumes an extremely high formation permeability. An 8 cm thick cement sheath loses all its pore pressure in their calculations as the cement's permeability becomes very low. However, the results clearly show that the pore pressure may not go to zero in some cases which should help maintain the stress levels in cement, all else being equal. In most cases, the sealing performance of cement is of interest against low permeability formations, such as a caprock. Such formations likely will not supply enough water to the cement sheath to maintain its pore pressure, at least in the short term. Therefore, the cement stress evolution in the absence of water is the more pressing question.

### Axial boundary condition

The model in this work assumes zero displacement at the top and bottom surfaces of cement (plane strain). This is different from the constant pressure boundary condition in the experiments conducted by Meng et al. <sup>25</sup>. When the cement is placed in the annulus, the top of cement is exposed to fluid pressure. Therefore, the constant pressure boundary condition is reasonable at the top of the cement sheath. The cement sheath is typically several hundreds of meters long, with two interfaces against the casing and the formation. As the cement develops strength, the friction forces on both interfaces of cement limit axial movement of the cement sheath. This limits the reach of the constant pressure boundary condition to the very top of the cement sheath. We have investigated the boundary condition using 3D models previously

(not shown here). The results indicate that the constant pressure boundary is only applicable to the top few meters of the cement sheath. The majority of the cement sheath experiences approximately a plane strain boundary condition. This exacerbates the stress drop observed in the  $^{25,26}$  data as the top pressure in their small-scale experiments helps maintain a higher radial stress. As the cement's pore pressure drops, the material tends to pull away from all interfaces (including the axial). The plane strain condition in the axial direction means no displacement or sliding in the axial direction. This leads to tensile stresses (due to pore pressure drop) in the axial direction which is released by disking cracks  $^5,$  which are commonly observed in large scale tests  $^{11,44}.$ 

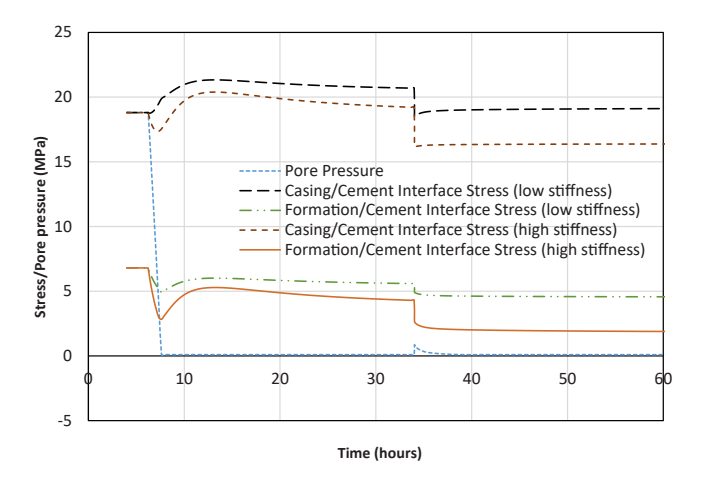
### Formation stiffness

Fig. 10 presents the cement interface stresses and pore pressure for the production well. The results are at a depth of 1200 m for the cement sheath behind the surface casing. The formation at this depth is less stiff, with Young's modulus of 10 GPa, compared to 16 GPa at the depth of 2000 m (for the injection well). The cement's pore pressure drops to zero from an initial pressure of 19 MPa. This leads to a stress drop of 1 and 4 MPa at the inner and outer cement interface, respectively. The surface casing is cemented to the surface, as opposed to the production liner. This leads to a higher initial pressure difference between the slurry and formation fluid for the surface casing. This apparent increase in effective stress leads to a higher initial effective stress at the formation/ cement interface. As the cement pore pressure drops to zero, the stresses at both of cement's interfaces drop. However, at the base of the surface casing the stresses remain compressive. This reduces the likelihood of microannulus formation due to hydration shrinkage and the subsequent operations. The softer formation at this depth also contributes to a higher level of stress retainment.

Fig. 12 compares the results of the same analysis as in Fig. 10 with a formation Young's modulus of 3.5 instead of 10 GPa. The decline in the formation/cement interface stress is only 2 MPa, compared to a 4 MPa decline in interface stress with a stiffer 10 GPa formation. These results indicate that the cement will retain more of its initial stress if the formation is softer. The lower stiffness in the formation accommodates the cement shrinkage by radial displacement. This reduces the level of stress drop at cement interfaces.

### Inner versus outer microannulus

Cement can debond on the inner or outer interface. There may be some differences between the consequences of either interface debonding. The outer microannulus is not easily identified in logs and



**Fig. 12.** Comparison of cement interface stresses set against high stiffness (10 GPa Young's modulus) and low stiffness (3.5 GPa Young's modulus) formations.

may go undetected. Modelling provides insights as to which interface is more likely to fail. Overall, the outer microannulus has a higher likelihood of failing as it loses more stress during hydration. However, there is an intricate balance of factors that may lead to different outcomes. One such factor is the formation bond strength. Cement will likely bond well with permeable formations due to fluid exchange with formations such as carbonates or sandstones. This means that regardless of the higher stress drop, the formation interface can withstand higher tensile stresses. Meanwhile, class G cement does not bond well to the casing. Therefore, the casing interface may debond before the bond strength to the formation is overcome. In addition, casing pressure is typically lowered after cement placement or during production. This can shrink the casing and drop the stress at the casing/cement interface. Cement may not bond as well to sealing formations such as shales. This means an outer microannulus is more likely against such formations. This means that CBL data may show a debonded cement against sandstones while showing a seemingly good bond against shales while an outer microannulus is present. It should be noted that only one of the interfaces will likely remain open as the fluids will flow towards the path of least resistance and higher pressure in one microannulus will close the other.

Another confounding factor is formation creep. Shale and salt formations are known to creep at different rates. This means that over the long term these formations may close the microannulus and restore the radial stress in cement. The creep rates and the ultimate stress should be confirmed in the lab at in-situ temperatures. This may allow for higher injection pressures in case of storage reservoirs.

The opening of an outer microannulus in the present geothermal well leads to an open leakage pathway during the injection phase. Since the injection occurs in an aquifer, there is no risk of gas leakage through the microannulus. The water pressure around the well may rise during injection. This pressure increase may lead to upwards flow of water through the microannulus. However, the higher density and viscosity of water compared to gas means a relatively low leakage rate. A risk assessment on the on the consequence of water leakage along the wellbore is prudent. The estimation of well leakage through the microannulus will be covered in part II of this paper.

### Heat of hydration

In this work, we included the impact of heat of hydration in the analysis. Heat of hydration leads to an accelerated increase of cement temperature as it cures. Fig. 13 presents a comparison of results for the injector well with and without the heat of hydration. Fig. 13b shows the cement temperature and microannulus size at early times. The temperature profile after cement placement is higher if heat of hydration is considered. Drilling is resumed at the 48 h mark which drops the temperature due to mud cooling. In the case with heat of hydration, temperature reaches 72 C and drops to 51 C due to drilling. If heat of hydration is ignored, temperature drops from 65 C to 50 C. This means that the realistic temperature drop in cement is higher due to drilling and ignoring the heat of hydration underestimates the risk of microannuli development. Fig. 13a shows the cement interface stresses. If heat of hydration is considered, cement stresses rebound initially due to the temperature increase. However, as drilling resumes at the 48 h mark, the stress drop at cement interfaces is more significant for the case with heat of hydration. This is due to a higher temperature drop due to mud circulation. This confirms that neglecting the heat of hydration leads to the underestimation of microannuli likelihood and size after cement placement.

While the hot fluid production does not open a microannulus, the increase in cement stress may lead to shear or fatigue failure. Fig. 15 presents the stress path at the inner side of the cement for the producer. Similar to the injector well, during hydration both the deviatoric stress and effective mean pressure increase in this case to 9 and 12 MPa, respectively. The increase in temperature and the pause and resumption of production cycles the deviatoric stress in a range that remains inside

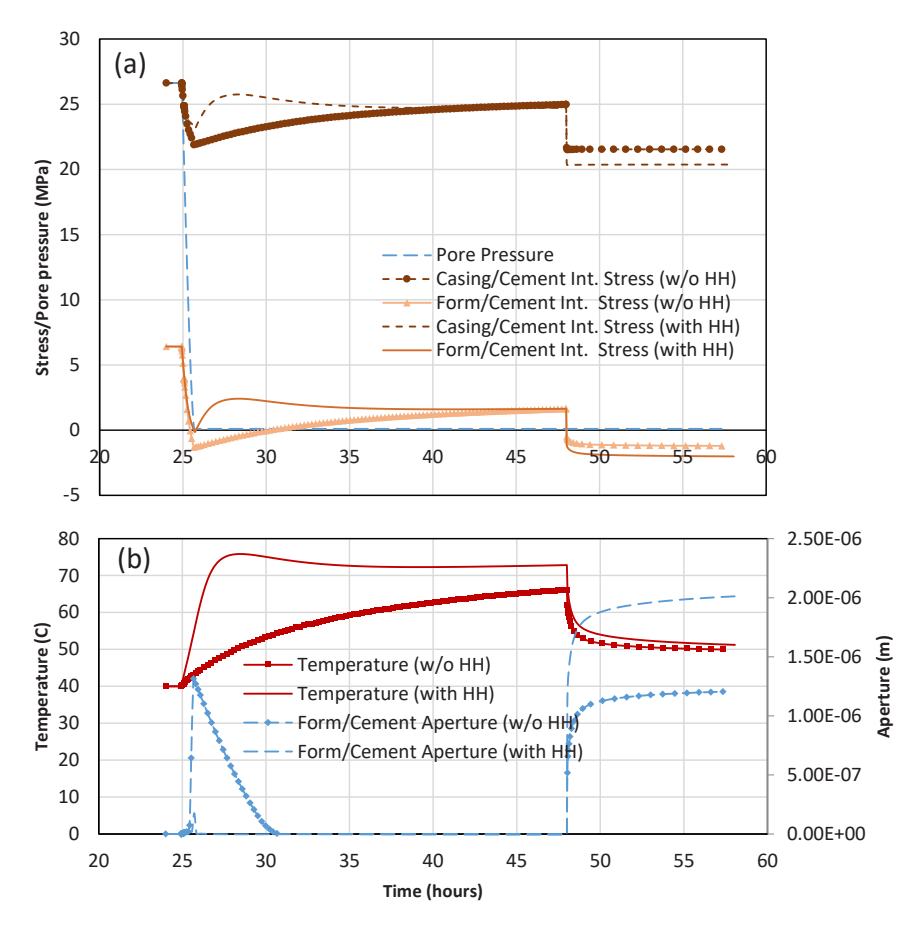
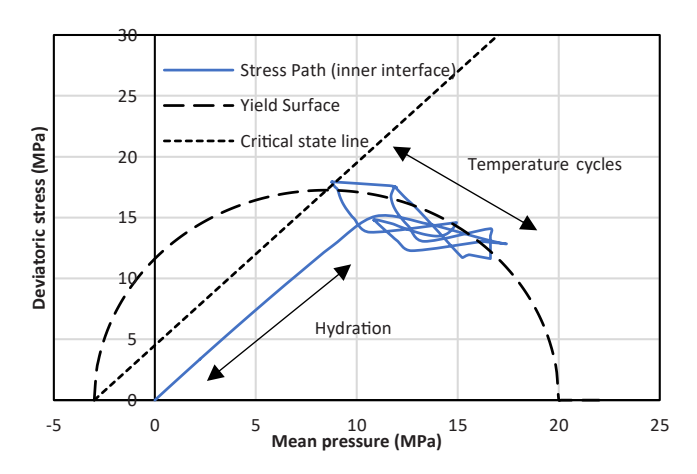


Fig. 13. Plot (a) shows the comparison between cement interface stresses in case of heat of hydration. Plot (b) shows the comparison of temperature and microannuli size, with and without consideration of heat of hydration.

the yield envelope. Therefore, the likelihood of shear failure is low. Cyclical accumulation of plastic strain can occur. However, the failure should be dilatative to be of concern for leakage. The stress paths presented here can be used to plan more representative cyclical loading tests. Typically, these tests are done in a triaxial apparatus by cycling the axial load. However, the stress path in those tests mimics only the hydration segment of the paths shown in Fig. 14 and Fig. 15.

# Cement failure

In addition to debonding, cement may undergo shear failure, tensile



 $\label{eq:problem} \textbf{Fig. 14.} \ \ \text{The stress path in the q-p space at the inner interface of cement for the injection well.}$ 

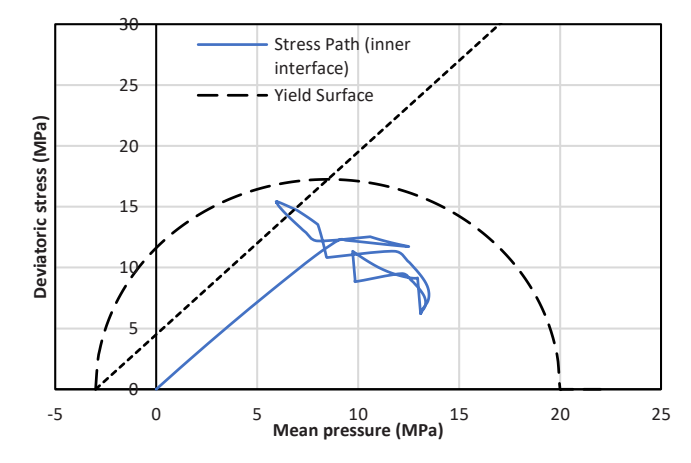


Fig. 15. The stress path in the q-p space at the inner and outer interface of cement for the producer well.

cracking, and cyclical damage. The impact of cyclical loads on cement is of interest as we expect a long operational life from geothermal wells. During their lifetime, there could be many instances of pause and resumption of injection which could expose cement to cyclical stress. Fig. 14 presents the stress path of cement for the injection well during the hydration and operational period. The stress in cement varies with the location in the cement sheath at a particular depth. We have plotted the stress at the inner surface of cement at the azimuth of  $0^{\circ}$  in the plane of the well. We observe that the stresses are generally slightly higher at the inner interface between the cement and casing. The stress paths are

plotted in the q-p space where q is the deviatoric stress (y-axis) and p is the effective mean pressure (x-axis). Immediately after cement placement, both the mean effective and deviatoric stresses are equal to zero. As hydration progresses and pore pressure drops the values increase linearly as indicated in Fig. 14. This continues until pore pressure reaches zero. For the inner cement this leads to an effective mean pressure of 10 MPa and a deviatoric stress of 15 MPa. The rest of the stress path is dominated by the impact of drilling, completion, and cold fluid injection.

Fig. 14 also illustrates the Modified Cam-Clay yield envelope and critical state line as reported by Soustelle et al. 41. The cement stress path surpasses the yield envelope during the operations which means plastic strains will be accumulated in cement. However, the failure is on the wet side of the envelope (right side of the critical state line) which indicates a ductile failure. Under these conditions the cement failure compresses the matrix further and reduces the permeability. According to the MCC theory, failure on the dry side of the envelope (left of the critical state line) will lead to brittle failure and fracture development. The MCC plasticity is deemed to be more suitable and representative of cement rather than Mohr-Coulomb failure criteria that is typically used 45,5.

Repetitive temperature cycles may lead to further accumulation of plastic strains. However, as shown by Soustelle et al. <sup>41</sup>, the subsequent cycles accumulate smaller amounts of strain. In addition, the cycles continue to compress the cement further if the failure is not dilatative. Therefore, under the mild stress conditions for the present case study, we do not deem the cyclical damage to be significant. It should be noted that the yield envelope shown in Fig. 14 is for cement at room temperature while the stress path is at 80 C. Therefore, experiments at higher temperatures are needed to improve the confidence in this assessment.

While the hot fluid production does not open a microannulus, the increase in cement stress may lead to shear or fatigue failure. Fig. 15 presents the stress path at the inner side of the cement for the producer. Similar to the injector well, during hydration both the deviatoric stress and effective mean pressure increase in this case to 9 and 12 MPa, respectively. The increase in temperature and the pause and resumption of production cycles the deviatoric stress in a range that remains inside the yield envelope. Therefore, the likelihood of shear failure is low. Cyclical accumulation of plastic strain can occur. However, the failure should be dilatative to be of concern for leakage. The stress paths presented here can be used to plan more representative cyclical loading tests. Typically, these tests are done in a triaxial apparatus by cycling the axial load. However, the stress path in those tests mimics only the hydration segment of the paths shown in Fig. 14 and Fig. 15.

### Cement stress evolution

The initial state of stress in cement depends on a complex set of parameters. Estimating the stress is required to calculate the size of the microannuli and the potential resulting leakage risk in wells. The following is a summary of the insights from the present study:

**Slurry pressure:** Higher slurry pressure increases the initial level of cement stress before the percolation threshold. This increases the ultimate remaining stress after the pore pressure drop in cement. Therefore, a higher slurry pressure should improve the cement's sealing performance, all else being equal.

Cement and formation mechanical properties: The stress drop in cement is mainly due to the pore pressure loss. The cement matrix will shrink due to the pore pressure drop. A softer cement matrix reduces the level of stress drop. In addition, a less stiff formation (lower Young's Modulus) reduces the stress drop in cement by providing more efficient confinement. A lower formation and cement stiffness should improve the sealing performance of cement, all else being equal.

**Axial boundary condition:** It is more likely that most of the cement sheath experiences a plane strain boundary condition as opposed to a constant pressure boundary. This has implications on the stress drop

levels due to hydration and experiments and modelling should reflect that

Water availability: An external water source can help maintain cement's pore pressure and contain stress drop. Highly permeable formations may be able to provide that. However, the sealing performance of cement is of interest against the sealing formations not against permeable formations. Therefore, the critical elements of the cement sheath likely lose their pore pressure, at least initially. Over the long term, the pore pressure in cement may rebound. However, the cement matrix may not expand as much as the hydrated cement is much stiffer than the young cement.

### Conclusions

In this paper, we outline a methodology to incorporate cement's hydration reactions in a staged finite element well integrity model. This method allows for a more accurate estimation of the initial cement stresses immediately after curing. Cement interface stresses determine the likelihood of debonding which can lead to well leakage. The methodology considers cement's hydration rate, evolution of the mechanical properties, and chemical shrinkage. The input parameters are all independently measured in different experimental studies from the literature. The model predictions of pore pressure, radial stress, and bulk shrinkage are verified by comparing them with lab experiments from the literature.

A case study is presented based on a geothermal doublet in the Netherlands. The analysis is conducted for the production liner of the injection well and the surface casing of the production well. The results at the bottom of the liner show high likelihood of debonding due to the injection of cold fluids and hydration shrinkage. The aperture of the resulting outer microannulus is expected to be  $60 \mu m$ . The surface casing shows more resilience to debonding as stresses remain compressive. The heat of hydration increases the cement temperature which could lead to a more detrimental impact of subsequent drilling operations. The stress path of cement is presented which can be used in future experimental studies to assess the potential cyclical damage. A softer formation and higher slurry pressure either due to a heavier or longer cement column can improve the initial stress of cement. This analysis can be conducted at several points along a well to determine the risk of debonding and leakage. The modelling study provided in this work allows for quantitative assessment of cement's sealing performance along a well. The part II of this work will focus on estimating potential leakage rates based on the modelling outlined here.

### **Declaration of Competing Interest**

The authors declare that they have no known competing financial interests or personal relationships that could have appeared to influence the work reported in this paper.

### **Data Availability**

Data will be made available on request.

### Acknowledgements

This work was partially supported by the Geothermica Test-CEM project. The Dutch contribution to the TEST-CEM project was carried out with a subsidy from the Ministry of Economic Affairs and Climate, Top Sector Energy subsidy scheme implemented by the Netherlands Enterprise Agency (RVO).

### References

- Agofack N, Ghabezloo S, Sulem J. Chemo-poro-elastoplastic modelling of an oilwell cement paste: macroscopic shrinkage and stress-strain behaviour. Cem Concr Res. 2020:132. 106046.
- Agofack N, Ghabezloo S, Sulem J, Garnier A, Urbanczyk C. Experimental investigation of the early-age mechanical behaviour of oil-well cement paste. Cem Concr Res. 2019;117:91–102.
- Bentz DP, Lura P, Roberts JW. Mixture proportioning for internal curing. Concr Int. 2005;27(2):35–40.
- Bernard O, Ulm F-J, Lemarchand E. A multiscale micromechanics-hydration model for the early- age elastic properties of cement based materials. Cem Concr Res. 2003; 33(9):1293-1309
- Bois A-P, Garnier A, Galdiolo G, Laudet J-B. Use of a mechanistic model to forecast cement-sheath integrity. SPE Drill Complet. 2012;27(02):303–314. https://doi.org/ 10.2118/139668-PA.
- Bois A-P, Garnier A, Rodot F, Sain-Marc J, Aimard N. How To prevent loss of zonal isolation through a comprehensive analysis of microannulus formation. SPE Drill Complet. 2011;26(01):13–31.
- Bois AP, Vu MH, Noël K, et al. Evaluating cement-plug mechanical and hydraulic integrity. SPE Drill Complet. 2019;43(2):92–102.
- Bosma, M., K. Ravi, W. van Driel, & G.J. Schreppers (1999). Design Approach to Sealant Selection for the Life of the Well. In Proceedings of the SPE Annual Technical Conference and Exhibition, 3–6 October, Houston, Texas.
- Bourissai M, Meftah F, Brusselle-Dupend N, Lécolier É, Bonnet G. Évolution des propriétés élastiques d'une pâte de ciment pétrolier au très jeune âge dans des conditions HP/HT: Caractérisation expérimentale et modélisation. Oil Gas Sci Technol. 2013;68(3):595–612.
- Chenevert ME, Shrestha BK. Chemical shrinkage properties of oilfield cements. SPE Drill Eng. 1991;6(1):37–43.
- Corina AN, Moghadam A. The sealing performance of cement sheaths under thermal cycles for low-enthalpy geothermal wells. *Energies*. 2024;17(1):239.
- Dillenbeck RL, Heinold T, Rogers MJ, Mombourquette IG. The effect of cement heat of hydration on the maximum annular temperature of oil and gas wells. SPE Drill Complet. 2003;18(04):284–292. https://doi.org/10.2118/87326-PA.
- Dusseault MB, Bruno MS, Barrera J. Casing shear: causes, cases, cures. SPE Drill Complet. 2001;9:8–107.
- Frash LP, Carey JW. Engineering prediction of axial wellbore shear failure caused by reservoir uplift and subsidence. SPE J. 2018;23(4):1039–1066.
- Ghabezloo S. Association of macroscopic laboratory testing and micromechanics modelling for the evaluation of the poroelastic parameters of a hardened cement paste. Cem Concr Res. 2010;40(8):1197–1210.
- Ghabezloo S, Sulem J, Guedon S, Martineau F, Saint-Marc J. Poromechanical behaviour of hardened cement paste under isotropic loading. Cem Concr Res. 2008; 38:1424–1437.
- Gray KE, Podnos E, Becker E. Finite-element studies of near-wellbore region during cementing operations: part I. SPE Drill. Completion. 2009;24(01):127–136.
- Guner D, Ozturk H, Erkayaoglu M. Investigation of the elastic material properties of Class G cement. Struct Conc. 2017;18:84–91.
- Jiang L, Zhang Y, Hu C, Li Z. Calculation of elastic modulus of early-age cement paste. Adv Cem Res. 2012;24(4):193–201.
- Lee BJ, Kee SH, Oh T, Kim YY. Evaluating the dynamic elastic modulus of concrete using shear-wave velocity measurements. Adv Mater Sci Eng 2017. 2017.
- Levine, D.C., Thomas, E.W., Bezner, H.P. et al. (1979). Annular Gas Flow after Cementing: A Look at Practical Solutions. In Proc. SPE Annual Technical Conference and Exhibition, Las Vegas, Nevada, USA.
- Li Z, Vandenbossche JM, Iannacchione AT, Vuotto A. Characterization of oil well cement performance during early hydration under simulated borehole conditions. SPE J. 2021;26(06):3488–3504.
- Lin F, Meyer C. Hydration kinetics modeling of Portland cement considering the
  effects of curing temperature and applied pressure. Cem Concr Res. 2009;39(4):
  255–265.
- 24. Mechelse E. The in-situ stress field in the Netherlands: Regional trends, local deviations and an analysis of the stress regimes in the northeast of the Netherlands (MSc thesis). Netherlands: Department of Geoscience & Engineering, Delft University of Technology; 2017.
- Meng M, Frash LP, Carey JW, Li W, Welch NJ, Zhang W. Cement stress and microstructure evolution during curing in semi-rigid high-pressure environments. Cem Concr Res. 2021;149, 106555.
- Meng, M., Frash, L., Carey, J.W., Niu, Z., & Zurich, E.T.H. (2021b). Predicting Cement-Sheath Integrity with Consideration of Initial State of Stress and Thermoporoelastic Effects. December 2020.
- Moghadam A, Loizzo M. Cement Integrity Assessment Using a Hydration-Coupled Thermo-Mechanical Model. SPE Offshore Europe Conference Proceedings,; 2023. https://doi.org/10.2118/215497-MS.

- Moghadam A, Peters E, Nelskamp S. Gas leakage from abandoned wells: a case study for the Groningen field in the Netherlands. Int J Greenh Gas Control. 2023;126, 103906
- Moghadam A, Vaisblat N, Harris NB, Chalaturnyk R. On the magnitude of capillary pressure (suction potential) in tight rocks. J Pet Sci Eng. 2020;190:107–133.
- 30. Nelson EB, Guillot D. Well Cementing. Schlumberger,; 2006. ISBN 9780978853006.
- Orlic, B., Moghadam, A., Brunner, L., van Unen, M., Wojcicki, A., Bobek, K., van der Valk, K., & Wollenweber, J. (2021). A Probabilistic Well Integrity Analysis Workflow for Leakage Risk Assessment: Case Studies for Shale Gas and Re-Use for CCS. In Proceedings of the 15th Greenhouse Gas Control Technologies Conference 2020 (GHGT-15). March 16–21, UAE.
- Osborn SG, Vengosh A, Warner NR, Jackson RB. Methane contamination of drinking water accompanying gas-well drilling and hydraulic fracturing. *Proc Natl Acad Sci* USA. 2011;108(20):8172–8176.
- Pang X, Bentz DP, Meyer C, Funkhouser GP, Darbe R. A comparison study of portland cement hydration kinetics as measured by chemical shrinkage and isothermal calorimetry. Cem Concr Compos. 2013;39:23–32.
- 34. Pang X, Sun L, Sun F, Zhang G, Guo S, Bu Y. Cement hydration kinetics study in the temperature range from 15 °C to 95 °C: Cement and Concrete Research. 2021;148, 106552
- Pichler B, Hellmich C, Eberhardsteiner J. Spherical and acicular representation of hydrates in a micromechanical model for cement paste: prediction of early-age elasticity and strength. *Acta Mech.* 2009;203:137–162.
- Rabbat BG, Russell HG. Friction Coefficient of Steel on Concrete or Grout. J Struct Eng. 1985;111(3).
- Reddy BR, Xu Y, Ravi K, Gray D, Pattillo PD. Cement-shrinkage measurement in oilwell cementing - a comparative study of laboratory methods and procedures. SPE Drill Complet. 2009;24(1):104–114.
- Romero J, Loizzo M. The importance of hydration heat on cement strength development for deep water wells. SPE Annu Tech Conf Exhib (p SPE-62894-MS). 2000. https://doi.org/10.2118/62894-MS.
- Saint-Marc, J., A. Garnier, & A.-P. Bois (2008). Initial State of Stress: The Key to Achieving Long-Term Cement-Sheath Integrity. In Proceedings of the SPE Annual Technical Conference and Exhibition, Denver, Colorado, USA, September 2008.
- Schout G, Griffioen J, Hassanizadeh SM, Cardon de Lichtbuer G, Hartog N.
   Occurrence and fate of methane leakage from cut and buried abandoned gas wells in the Netherlands. Sci Total Environ. 2019;659:773–782.
- Soustelle, V., Moghadam, A., & Corina, A.N., (2023). Modified Cam-clay Model Parameters for Well-cement. Paper SPE presented at SPE EuropEC - Europe Energy Conference, Vienna, Austria. SPE-214393-MS.
- Sun L, Pang X, Yan H. Hydration kinetics of oil well cement in the temperature range between 5 and 30°C. Front. Mater. 2022;9, 985332. https://doi.org/10.3389/ fmats.2022.985332.
- Teodouri C, Amani M, Yuan Z, Schubert J, Kosinowsli C. Investigation of the mechanical properties of class G cement and their effect on well integrity. *Int J Eng Appl Sci.* 2013;3(2):1–7.
- Therond E, Bois A-P, Whaley K, Murillo R. Large-scale testing and modeling for cement zonal isolation in water-injection wells. SPE Drill. Completion. 2017;32(04): 290–300
- Thiercelin M, Baumgarte C, Guillot D. A soil mechanics approach to predict cement sheath behavior. SPE/ISRM Rock Mech Pet Eng (p SPE-47375-MS). 1998. https://doi. org/10.2118/47375-MS.
- Thiercelin MJ, Dargaud B, Baret JF, Rodriquez WJ. Cement design based on cement mechanical response. SPE Drill Complet. 1998;13(04):266–273.
- Ulm F-J, Constantinides G, Heukamp FH. Is concrete a poromechanics material? a multiscale investigation of poroelastic properties. *Mater Struct*. 2004;37(265):43–58.
- Van Breugel K. Numerical simulation of hydration and microstructural development in hardening cement-based materials:(I) theory. Cem Concr Res. 1995;25(2): 319–331.
- Wolterbeek TKT, Cornelissen EK, Hangx SJT, Spiers CJ. Impact of downhole pressure and fluid-access on the effectiveness of wellbore cement expansion additives. Cem Concr Res. 2021;147, 106514.
- Wolterbeek TKT, Hangx SJT. The thermal properties of set Portland cements a literature review in the context of CO<sub>2</sub> injection well integrity. *Int J Greenh Gas Control*. 2023;126(December 2022)), 103909. https://doi.org/10.1016/j. ijggc.2023.103909.
- 51. Zaoui A. Continuum micromechanics: survey. J Eng Mech. 2002;128(8):808–816.
- Zhang W, Eckert A, Hilgedick S, Goodman H, Meng M. Wellbore integrity: an integrated experimental and numerical study to investigate pore pressure variation during cement hardening under downhole conditions. SPE J. 2022;27(01):488–503. https://doi.org/10.2118/208574-PA.
- 53. Zhang W, Eckert A. Micro-annulus generation under downhole conditions: insights from three-dimensional staged finite element analysis of cement hardening and wellbore operations. J Rock Mech Geotech Eng. 2020;12(6):1185–1200.
- Zhang T, Gao P, Luo R, Guo Y, Wei J, Yu Q. Measurement of chemical shrinkage of cement paste: comparison study of ASTM C 1608 and an improved method. *Constr Build Mater*. 2013;48:662–669.